PAPER

Check for updates

Cyano-bridged {Fe$_2$Co} assemblies showing metamagnetic transition and a magnetocaloric effect†

Yu-Jing Gao,[a] Ji-Peng Luo, [b] Nan Yin,[b] Quan Shi, *[b] Yin-Shan Meng *[a,c] and Tao Liu *[a,c]

The investigation of magnetic materials featuring unconventional magnetic topologies represents a forefront research area in the interdisciplinary fields of physics, chemistry, and materials science. Such systems hold considerable promise for applications in strongly correlated electron systems, spintronic devices, magnetic memory technologies, and magnetocaloric applications. Among them, cyano-bridged Prussian blue analogues (PBAs) have emerged as a prominent class of molecular magnetic materials, offering a versatile platform for the systematic modulation of magnetic interactions and topological architectures through the rational selection of paramagnetic metal centers and auxiliary ligands. Herein, we report two heterometallic molecular magnets based on tricyanoferrate bridges, namely, [(PzTp)Fe(CN)$_3$]$_2$[Co(dypu)]·H$_2$O (**1**) and (Tp*)[Fe(CN)$_3$]$_2$[Co(dypu)]·H$_2$O (**2**) (dypu = 1,3-di(pyridin-4-yl)urea), which exhibit field-induced magnetic phase transition. Structural characterization shows that compounds **1** and **2** exhibit one-dimensional double-zigzag chains, further connected into a two-dimensional network by the ditopic dypu ligand. Magnetic analysis reveals ferromagnetic coupling between the cyano-bridged Fe^{III} and Co^{II} centers in compound **1**, whereas antiferromagnetic coupling occurs in **2**. Interestingly, variable-temperature and variable-field magnetic susceptibility measurements reveal notable magnetic structure transitions in compound **1**: (i) from spin-canted antiferromagnetism (AFM) to nearly collinear AFM at a critical field (H_{C1}) of 3.5 kOe, followed by (ii) a transition to a nearly ferromagnetic (FM) alignment at a second critical field (H_{C2}) of 18 kOe. Notably, a significant magnetocaloric effect is observed during the phase transition, with the change in entropy (ΔS) reaching 23.22 J K^{-1} kg^{-1}. This study underscores that the rational modulation of auxiliary ligands enables the tuning of diverse magnetic interactions and structural topologies and advances the understanding of magneto-structural correlations in molecular magnetic systems.

Introduction

Materials exhibiting field-induced magnetic phase transitions have attracted increasing attention in both materials science and condensed matter physics, owing to their significant potential for application in high-efficiency magnetic refrigeration,[1–3] magnetoresistive sensors,[4–7]

magnetostriction,[8–12] non-volatile magnetic memory,[13] and spintronic devices.[14] Such field-induced magnetic phase transitions originate from the competition between intrinsic spin interactions and external magnetic fields. For molecular magnetic materials, the spin configuration of the ground state is determined by the ground state of spin centers, all possible exchange interactions between them, single-ion magnetic anisotropies, and Zeeman interactions. When an external magnetic field is applied, it perturbs these competing interactions, sometimes resulting in metamagnetic transitions—abrupt changes in magnetization caused by field-induced spin realignment. Typically, the giant magnetocaloric effect (GMCE) is sometimes associated with field-driven phase transitions, enabling magnetic refrigeration through magnetization–demagnetization cycles.

Traditional inorganic metamagnetic materials have exhibited significant magnetocaloric effects,[15–19] whereas such giant magnetocaloric effects in molecular magnetic materials have not yet garnered broad attention. In contrast to inorganic

[a]*State Key Laboratory of Fine Chemicals, Frontier Science Center for Smart Materials, School of Chemical Engineering, Dalian University of Technology, No. 2 Linggong Road, Dalian 116024, P. R. China. E-mail: mengys@dlut.edu.cn, liutao@dlut.edu.cn*

[b]*Thermochemistry Laboratory, Dalian Institute of Chemical Physics, Chinese Academy of Sciences, Dalian Technology Innovation Center for Energy Materials Thermodynamics, Liaoning Province Key Laboratory of Thermochemistry for Energy and Materials, Dalian 116023, P. R. China. E-mail: shiquan@dicp.ac.cn*

[c]*Liaoning Binhai Laboratory, Dalian 116023, P. R. China.*

†Electronic supplementary information (ESI) available. CCDC 2457492 and 2457493. For ESI and crystallographic data in CIF or other electronic format see DOI: https://doi.org/10.1039/d5dt01187f

metamagnetic compounds, molecule-based systems offer distinct advantages owing to their well-defined crystal structures and tunable exchange interactions. These interactions can be precisely modulated by adjusting magnetic centers, ligands, and/or weak intermolecular interactions, making them particularly promising for the study of magnetic phase transitions.[20–23] Molecule-based metamagnetic materials are predominantly found in short-bridge-connected homo- or hetero-metallic coordination compound systems,[24–37] typically exhibiting strong magnetic coupling within one-dimensional chains and weak interactions between chains or layers. By systematically manipulating key factors such as cationic anisotropy, magnetic exchange interactions, and lattice distortions, the metamagnetic behavior of these materials can be altered.

In the last two decades, cyano-bridged Prussian blue molecular analogs have garnered significant attention due to their stimuli-responsive electron transfer, spin crossover, and other switchable properties. Additionally, the diverse cyano-bridge units enable the formation of variable molecular topologies and potentially intriguing magnetic properties. Among cyano-bridged bimetallic assemblies, ligand-modified tricyanide units $[Fe^{III}L(CN)_3]^-$ (L = tridentate ligand) exhibit tunable structures, where the nuclearity and dimensionality of the topological frameworks can be finely controlled at the molecular level. Notably, one of the well-studied building blocks is the tricyanoferrate anion, $[Tp^RFe^{III}(CN)_3]^-$ (Tp^R = poly(pyrazolyl)borate), which demonstrates considerable uniaxial magnetic anisotropy along its C_3 rotational axis (approximately along the B···Fe vector), making it an excellent candidate for constructing molecular magnets with interesting magnetic topologies.[38,39] In this work, we constructed compound **1** ([Fe(PzTp)(CN)$_3$]$_2$[Co(dypu)]·H$_2$O) [PzTp = tetrakis(pyrazolyl)borate] and compound **2** ([Fe(Tp*)(CN)$_3$]$_2$[Co(dypu)]·H$_2$O) [Tp* = hydridotris(3,5-dimethylpyrazol-1-yl)borate], by utilizing different ligand-modified tricyanide units in combination with a single-ion anisotropy Co^{II} center. Their crystal structure, magnetism, and magnetic topological structure were characterized and discussed in detail.

Experimental

Materials and methods

Synthesis of compounds. All reagents and solvents were obtained with analytical purity from commercial suppliers and used without further purification. Cautionary note: Co(ClO$_4$)$_2$·6H$_2$O is potentially explosive. It should be prepared in small quantities and handled with care.

[Fe(PzTp)(CN)$_3$]$_2$[Co(dypu)]·H$_2$O (1). A 1.0 mL aqueous solution that contained 0.05 mmol of Co(ClO$_4$)$_2$·6H$_2$O was placed at the bottom of a test tube, and a mixed solution of methanol and water (1 : 1, v/v, 3 mL) was gently layered on the top of the solution and then 1.0 ml of methanol solution that contained 0.05 mmol of (Bu$_4$N)$_3$[Fe(pzTp)(CN)$_3$]·and 0.1 mmol of the ligand L (dypu = 1,3-di(pyridin-4-yl)urea) was added as the

third layer. Orange-brown flake crystals of **1** were obtained after keeping in the dark for a few months. Yield: 59% based on Co(ClO$_4$)$_2$·6H$_2$O. Elemental analysis: calcd (found) for C$_{41}$H$_{36}$B$_2$CoFe$_2$N$_{26}$O$_2$ (%): C 43.96 (43.74), H 3.21 (3.09), N 32.53 (32.78).

[Fe(Tp)(CN)$_3$]$_2$[Co(dypu)]·H$_2$O (2).* Red-brown needle crystals of **2** were prepared in a similar way to **1** but using (Bu$_4$N)$_3$[Fe(Tp*)(CN)$_3$]. Yield: 43% based on Co(ClO$_4$)$_2$·6H$_2$O. Elemental analysis: calcd (found) for C$_{47}$H$_{58}$B$_2$CoFe$_2$N$_{22}$O$_3$ (%): C 48.16 (48.42), H 4.95 (4.75), N 26.30 (26.02).

Physical measurements

Structure determinations and refinements. Single-crystal X-ray diffraction data were collected on a Bruker D8 VENTURE CMOS-based diffractometer (Bruker AXS Company, Karlsruhe, Germany) (Mo-Kα radiation, λ = 0.71073 Å) using the SMART and SAINT programs. Final unit cell parameters were based on all observed reflections from the integration of all frame data. The structures were solved with the ShelXT structure solution program using intrinsic phasing and refined with the ShelXL refinement package, using least-squares minimization that was implemented in Olex2.

Elemental analyses. Elemental analyses of **1** and **2** were performed on an Elementar Vario EL III analyzer.

Powder X-ray diffraction (PXRD). Powder X-ray diffraction (PXRD) patterns were obtained on a Rigaku 2400 diffractometer at RT with CuK$_\alpha$ radiation (λ = 1.5418 Å) with a step size of 0.02° and a scanning rate of 10° min^{-1}. The microcrystalline samples were carefully deposited onto the center of the glass sample stage, ensuring a uniform coverage and distribution over the entire area.

Magnetic studies. Magnetic measurements were carried out with a PPMS magnetometer using polycrystalline samples. The temperature-dependent magnetic susceptibility data were recorded with a sweeping rate of 2 K min^{-1} above 10 K and 0.5 K min^{-1} in the temperature range of 2–10 K. Magnetic measurements were conducted on polycrystalline samples encapsulated in polycarbonate capsules with parafilm seals. Data were corrected for the diamagnetic contribution calculated from Pascal constants and the background from the parafilm and capsules.

Heat capacity measurement. The low temperature heat capacities of **1** were measured using a Quantum Design PPMS based on a relaxation calorimetric method in the temperature range of T = 1.9 to 300 K. The standard uncertainty of the PPMS heat capacity measurement was estimated, by measuring the heat capacities of a high purity copper pellet, a-Al$_2$O$_3$ (SRM720) and benzoic acid (SRM39 j) and comparing the measured data to the corresponding literature values, to be ±3% in the temperature range from 1.9 to 20 K and ±1% from 20 to 300 K. Powder samples were prepared into a pellet with a diameter of 3 mm and a height of 1–2 mm, by compressing the mixture of powders and copper stripes in a copper cup together. The sample coupling in the thermal relaxation process was found to be better than 95%, suggesting that good

Results and discussion

Crystal structures

Single-crystal X-ray diffraction at 120 K reveals that **1** crystallizes in the monoclinic space group $C2/c$. The asymmetric unit contains half of the [Fe(pzTp)(CN)$_3$]$_2$[Co(dypu)] (dypu = 1,3-di(pyridin-4-yl)urea) fragment and half of the lattice solvents (Fig. 1a). All of the Fe(III) and Co(II) ions are located in the distorted octahedral coordination sphere, with an Fe–C/N bond length of 1.903(0)–1.913(6) Å and a Co–N bond length of 2.122(4)–2.155(4) Å, typical for those observed in the related LS Fe(III) or HS Co(II) species. The cyano-bridged {Fe$_2$Co} double-zigzag chains are arranged in the bc plane, connected by ligands and stacked along the a axis, forming a 2D network as a whole in the ac plane. The O atoms of the adjacent ligands are opposite in the b-axis direction (Fig. 1b). The extension of the 2D planar structure into a 3D framework is through $\pi\cdots\pi$ stacking by the pyrazolyl groups of the PzTp ligands (Fig. 1c). The intrachain Fe$\cdots$Co distances are 4.9322(5) Å and 4.9548(5) Å, while the interchain Co$\cdots$Co distance is 14.6746(21) Å. Additionally, the interlayer $\pi\cdots\pi$ interactions are 3.355(0) Å, which leads to the nearest interlayer Fe$\cdots$Fe distance being 7.5579(8) Å. Notably, the intralayer metal–metal distances bridged by ligands are nearly twice as large as the interlayer metal–metal distances connected through robust interlayer $\pi\cdots\pi$ interactions (14.67 Å $vs.$ 7.56 Å). This substantial difference effectively isolates the potential magnetic interactions within the intralayer adjacent chains, while suggesting that the interlayer magnetic interactions between metals could be significantly stronger than those between the intralayer chains.

Compound **2** is synthesized by substituting the building block Tp* in place of PzTp, resulting in a modified structure (Fig. S1†). Compared to compound **1**, the steric hindrance of the building blocks in compound **2** along the a axis is reduced (Fig. 2a and b), which results in a less distorted tetragonal lattice, as illustrated in Fig. 2c. Additionally, the planar orientation of the dypu ligand also changes from the ab plane

(Fig. 2a and b) to the ac plane (Fig. 2d and e). Single-crystal X-ray diffraction at 120 K reveals that **2** crystallizes in the higher symmetry orthorhombic space group $Ibam$. The replacement of the building block has led to alterations in the distances between metals within the framework and the weak interactions between chains. Selective key bond lengths, bond angles, intermetallic distances, and interlayer interaction for **1** and **2** are presented in Table 1.
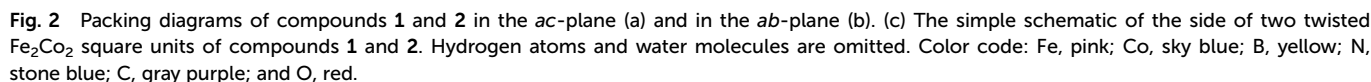
According to the different twist degrees of the Co–N≡C angle which deviate significantly from linearity in **1**, the cyano nitrogen atoms can be divided into two categories, namely N1 and N3. The cyano-bridge features a linear arrangement with respect to the Fe(III) center [Fe1–C1≡N1, 173.460(421)°; Fe1–C4≡N3, 173.209(466)°], while the bridge is more bent on the Co(II) site [C1≡N1–Co1, 148.7(4)°; C4≡N3–Co1, 147.7(4)°] (Fig. 2c). Evidently, compound **2** exhibits significantly less distortion, with a bond angle of 168.0°. Commonly, the parameter Σ can be used to evaluate the geometry deviation from the standard octahedral ligand field around a transition-metal ion, which is the sum of $|90 - \alpha|$ for the 12 cis-N–Co–N angles around the metal atom. For compound **1** at 120 K, the value of Σ_{Co} is 59.82. In contrast, the value of Σ_{Co} for compound **2** is 17.92, indicating that the CoN$_6$ octahedron in **1** undergoes larger distortion. The Jahn–Teller (JT) axes of iron and cobalt are positioned at an angle within the double-zigzag chains, leading to anisotropic spin-coupling interactions (Fig. 2c).

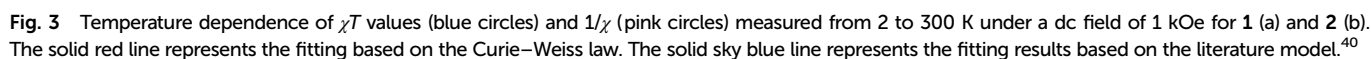### Magnetic characterization

The temperature-dependent susceptibilities of **1** and **2** were recorded under a direct current (dc) field of 1 kOe over the temperature range of 2–300 K (Fig. 3). The powder X-ray diffraction patterns for all of the complexes matched well with their SCXRD simulations (Fig. S2†), indicating the good purity of the samples. At 300 K, the χT value of **1** is 2.63 cm^3 mol^{-1} K, which is larger than the spin-only value of 4.10 cm^3 mol^{-1} K for the two Fe$_{LS}^{III}$ centers ($S = 1/2$, $g = 2$) and one Co$_{HS}^{II}$ center ($S = 3/2$, $g = 2$), reflecting the magnetic anisotropy of Co^{II}. Upon cooling, the χT value increases slowly between 300 and 80 K and then sharply below 80 K and the maximum of 11.8 cm^3 mol^{-1} K is observed at $T = 16$ K. Fitting of the data above 16 K
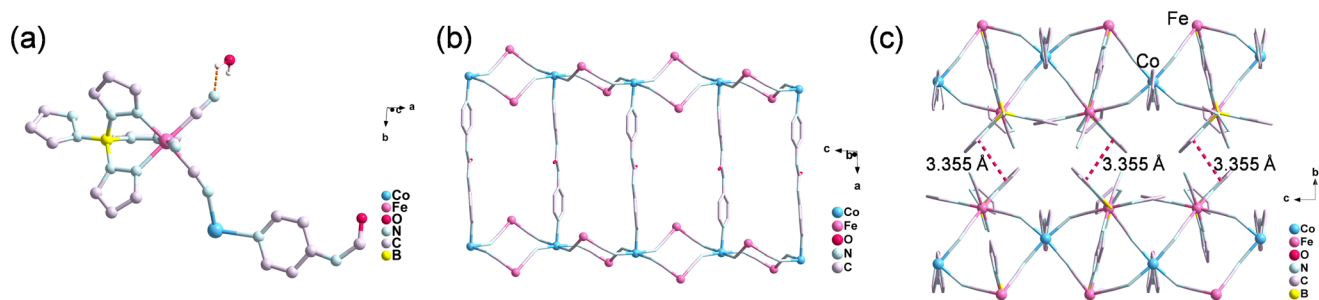
Fig. 1 (a) The asymmetric unit of compound **1**. Packing diagrams of compound **1** in the ac-plane (b) and in the bc-plane (c). Hydrogen atoms and water molecules are omitted. Color code: Fe, pink; Co, sky blue; B, yellow; N, stone blue; C, gray purple; and O, red.

Fig. 2 Packing diagrams of compounds **1** and **2** in the *ac*-plane (a) and in the *ab*-plane (b). (c) The simple schematic of the side of two twisted Fe$_2$Co$_2$ square units of compounds **1** and **2**. Hydrogen atoms and water molecules are omitted. Color code: Fe, pink; Co, sky blue; B, yellow; N, stone blue; C, gray purple; and O, red.

Table 1 Some key bond lengths, bond angles, and intermetallic distances for **1** and **2**

	Fe–C/N, Å	Co–N, Å	Co–N≡C	Intrachain Fe⋯Co distance, Å	Interchain Co⋯Co distance, Å	Interlayer Fe⋯Co distance, Å	Interlayer interaction	Σ_{Co}
1	1.90–1.91	2.12–2.15	148.7(4)°, 147.7(4)°	4.93, 4.95	14.67	7.56	π⋯π: 3.35 Å	59.82
2	1.92–1.94	2.13–2.16	168.0(4)°	5.16	14.78	9.47	C–H⋯π: 3.81 Å	17.92

Fig. 3 Temperature dependence of χT values (blue circles) and $1/\chi$ (pink circles) measured from 2 to 300 K under a dc field of 1 kOe for **1** (a) and **2** (b). The solid red line represents the fitting based on the Curie–Weiss law. The solid sky blue line represents the fitting results based on the literature model.[40]

according to the Curie–Weiss law gives the Weiss constant θ = 13.83 K, suggesting the considerable ferromagnetic coupling between the cyano-bridged Fe^{III} and Co^{II} centers, consistent

with the Goodenough–Kanamori rule that orthogonal metal orbitals (t$_{2g}$ and e$_g$) lead to ferromagnetic interaction.[41] To assess the exchange coupling interactions, the magnetic data

were fitted using the theoretical expression for isolated double chains proposed by Drillon *et al.*:

$$\chi = Ng^2\mu_B^2/2kT\{E[4\,\exp(K^+) + \cosh(K^+) + 1]$$
$$-8\,\cosh(K^+) - \cosh(K^-)\}/\{E[E - 2\,\cosh(K^+) - 2]\}$$

where $E = 2[\cosh(K^+) + \cosh(K^-) + 2]$, $K^+ = (J_1 + J_2)/2kT$, $K^- = (J_1 + J_2)/2kT$, and J_1 and J_2 represent the magnetic interactions within and between the trimers. The best fit of the experimental data in the range of 25 and 300 K yielded $J_1 = 14.0(9)$ cm^{-1} (20.3 K), $J_2 = 19.1(1)$ cm^{-1} (27.52 K), and $g = 3.17(8)$, with a consistency factor of 0.988. These J values indicate significant ferromagnetic coupling between the Fe^{III} and Co^{II} ions within the chains. The sharp peak of χT at low temperatures indicates a long-range magnetic ordering below 16 K. After that, the χT abruptly decreases to almost 0 cm^3 mol^{-1} K at 2 K. A further decrease in the $\chi T(T)$ plot, with the magnetic signal at the lowest temperature almost vanishing, suggests the presence of interlayer antiferromagnetic interactions leading to an antiferromagnetic ordering between ferromagnetic layers, with the expected cancellation of magnetic moments. This interpretation is also supported by the field-cooled magnetization curve for $H = 1$ kOe (Fig. S3a†), revealing the sharp maximum at $T_N = 16$ K, which determines the critical Néel temperature of the phase transition to the antiferromagnetically ordered state. Magnetic studies indicate that compound **2** shows AFM coupling ($\theta = -14.23$ K, $J = -8.8$ cm^{-1}) between the cyano-bridged Fe^{III} and Co^{II} centers. The small increase of the χT value at low temperatures indicates a ferrimagnetic ordering below 14 K, which may be caused by the noncancellation of magnetic moments between Fe^{III} and Co^{II} centers.

The isothermal field dependence of the magnetization for compounds **1** and **2** was measured at 2 K, with a magnetic field of up to 50 kOe (Fig. 4). The *M vs. H* curve for compound **1** exhibits a sigmoidal shape, with two critical magnetic fields (H_{C1} and H_{C2}) identified from the peak observed in the plot of the field dependence of the first derivative of magnetization (Fig. 4c). As the magnetic field increases, the magnetization initially increases slowly until 16 kOe, at which point an abrupt upturn occurs before gradually rising again to a maximum value of 2.5$N\beta$ at 50 kOe. This value does not approach the theoretical saturation magnetization of 5$N\beta$ per Fe$_2$Co unit, indicating the presence of a spin-canted AFM phase. A noticeable increase in magnetization, with a critical magnetic field $H_{C1} = 3.5$ kOe, is observed particularly below 9 K (Fig. 5), suggesting the presence of spontaneous magnetization, which is indicative of significant magnetic anisotropy originating from the single-ion anisotropy of the Co^{II} center. Further evidence for magnetic anisotropy in compound **1** is provided by the appearance of a hysteresis loop (Fig. 6). The canting angle is estimated to be approximately 8.1°, calculated using the expression $\sin\alpha = M_R/M_S$, where $M_R = 0.7N\beta$ is determined from the extrapolation of the linear portion of the magnetization curve at higher magnetic fields to a zero field, and M_S represents the saturation magnetization.

The critical magnetic field value of $H_{C2} = 18$ kOe is notably high among cyano-bridged molecular assemblies. The shortest interchain metal–metal distance of 14.67 Å is very large, which effectively minimizes interchain magnetic interactions, thereby providing the potential for single-chain magnet (SCM) behavior without a long-range magnetic ordering. However, no SCM properties are observed, as shown in Fig. S4.† The long-range magnetic ordering observed in this system is likely
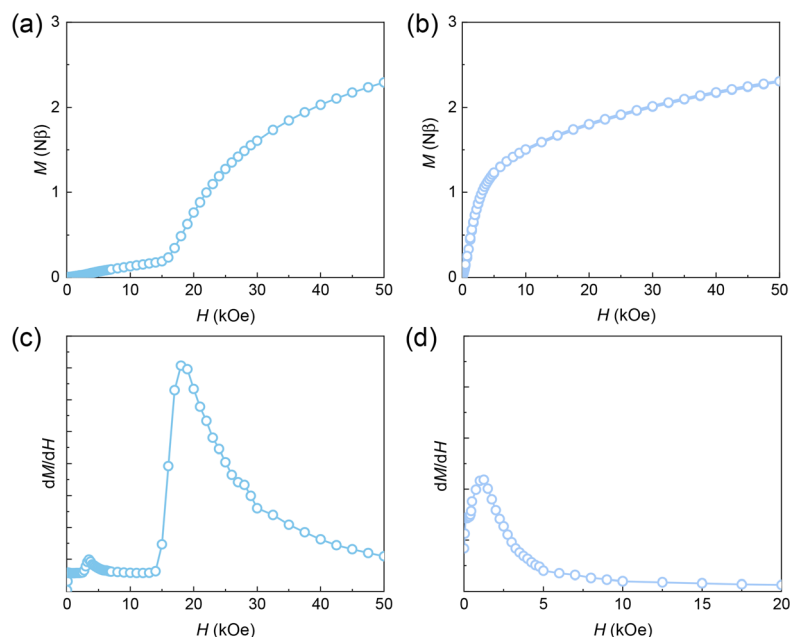

Fig. 4 The field dependence of magnetization at $T = 2$ K for **1** (a) and **2** (b), and field dependences of the first derivatives (c and d).
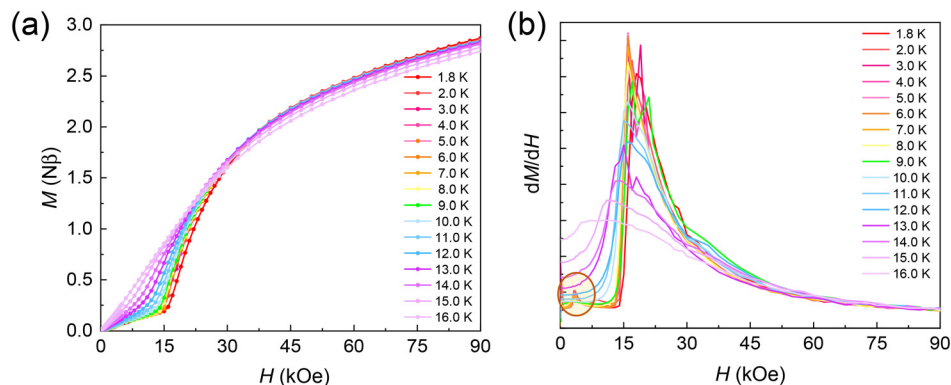
Fig. 5 (a) Field-dependent magnetization data for **1** at various temperatures. (b) The derivatives of the magnetization (dM/dH) for **1** at various temperatures.
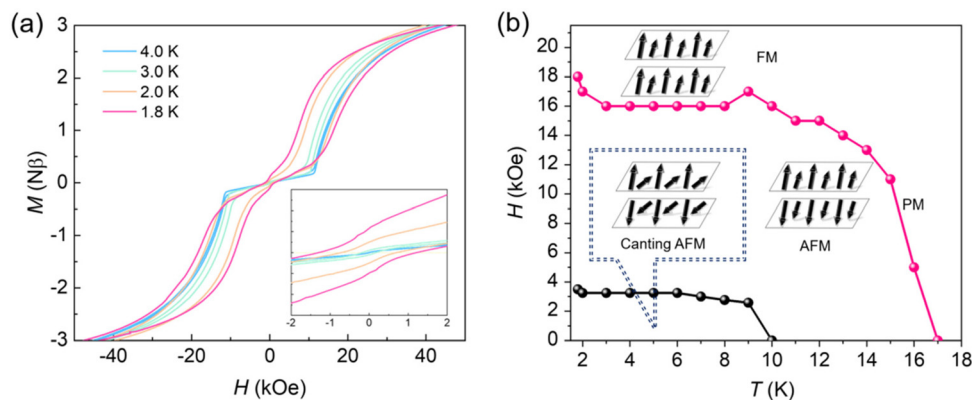

Fig. 6 (a) Hysteresis loops of **1** between −50 and 50 kOe at T = 1.8 K, 2.0 K, 3.0 K, and 4.0 K. (b) The magnetic phase diagram of **1**. The inset scheme shows the orientation of the magnetic moments for metal centers at different magnetic phases, where the square represents the magnetic layer.

attributed to the lateral $\pi\cdots\pi$ interactions between Fe^{III}-centered building blocks, mediated through the pyrrole rings of adjacent chains. These antiferromagnetic interactions propagate from the metal ions within the double-zigzag chains to the metal ions in the adjacent layers along the b-axis direction via the $\pi\cdots\pi$ interactions (Fig. 1c). Similar metamagnetic behavior has been observed in one-dimensional chain compounds, where $\pi\cdots\pi$ stacking interactions between aromatic rings on adjacent chains are responsible for the magnetic interactions.[40,42,43] The metamagnetic properties can be understood in the context of the crystal structure of compound **1**, where intrachain ferromagnetic coupling and interlayer antiferromagnetic interactions (J') mediated by the $\pi\cdots\pi$ stacking interactions exist. The high critical field suggests that J' is strong. In contrast, compound **2** exhibits a single magnetic phase transition at a transition field of 1.2 kOe (Fig. 4d), which is likely due to the interlayer antiferromagnetic to ferromagnetic phase transition, attributed to weak C–H$\cdots\pi$ stacking interactions (Fig. S1b, and S6b†).

The M $vs.$ H curves within the temperature range of 1.8–16 K and the magnetic field range of 0–90 kOe (Fig. 5) exhibit clear temperature dependence, with the critical magnetic fields for the metamagnetic transition gradually decreasing as

the temperature increases. The sigmoidal shape anomaly in the curves becomes less pronounced with the increase of temperature, which is characteristic of a metamagnet consisting of two ferromagnetic subnetworks coupled antiferromagnetically. The antiferromagnetic coupling can be overcome by the application of an external magnetic field, resulting in a transition of the ground state from an antiferromagnet to a ferromagnet. Notably, the magnetization change at 3.5 kOe disappears at 9 K, while the magnetization change at 18 kOe persists until 16 K. This behavior suggests a spin-canting phase, where the magnetic moments are canted before reaching the antiferromagnetic state. Combined with the observed metamagnetic behavior, this phenomenon is likely attributed to a hidden spin-canting phase arising from the non-collinear antiferromagnetic spin arrangement of the Fe^{III} and Co^{II} sublattices.

To gain further insight into the low-temperature magnetic behavior, zero-field-cooling (ZFC) and field-cooling (FC) magnetic susceptibility measurements were conducted under various applied magnetic fields. As shown in Fig. S5,† a sharp peak appears at 16 K in the ZFC-FC curves, which corresponds to the Néel temperature and indicates the onset of a long-range antiferromagnetic (AFM) ordering. The pronounced field dependence of susceptibility below this temperature strongly

indicates a field-induced magnetic phase transition. With increasing external field strength, the maximum in the χT curve progressively shifts to lower temperatures and eventually vanishes above $H = 30$ kOe, suggesting saturation of magnetization. Notably, at low fields below 4000 Oe and temperatures below 9 K, a gradual increase in χT with the increase of magnetic field strength is observed, consistent with the presence of a spin-canted AFM phase. Such field- and temperature-dependent magnetic properties reveal a distinct magnetic transition from a spin-canted AFM phase to a more collinear AFM phase. This progression indicates that the applied DC field initially suppresses intrachain spin canting, followed by the disruption of interlayer antiferromagnetic coupling, and finally inducing a field-driven metamagnetic transition from the AFM to the ferromagnetic (FM) phase.

Despite that compound **1** crystallizes in a centrosymmetric space group, there is no inversion center between adjacent magnetic ions, thus allowing for the presence of the Dzyaloshinskii–Moriya (DM) interaction. These antisymmetric exchange interactions can induce spin canting, resulting in weak ferromagnetism. To further probe the existence of a latent spin-canted phase arising from the non-collinear antiferromagnetic alignment between Fe and Co sublattices, detailed magnetic hysteresis measurements were conducted in the temperature range of 1.8–4 K, as depicted in Fig. 6a. At 1.8 K, compound **1** exhibits a characteristic butterfly-shaped hysteresis loop, with a coercive field of 1215 Oe originating from the canting state. As the temperature increases, the hysteretic loops become narrow and ultimately vanish above 4 K,

signifying a transition toward a more collinear antiferromagnetic ground state. The observed hysteresis loops display notable differences between the ascending and descending field branches at various temperatures, indicative of a first-order phase transition. This behavior is characteristic of canted antiferromagnets and reflects the emergence of weak spontaneous magnetization at low temperatures within a predominantly antiferromagnetic framework. Such magnetization arises from the incomplete cancellation of magnetic moments due to the slight misalignment of spins in different sublattices. Below the critical temperature, these uncompensated spins become correlated, establishing a long-range magnetic ordering with a ferromagnetic-like character superimposed on the underlying antiferromagnetic structure. Based on the differential analyses of the magnetization curves in Fig. 5 and S5,† a series of (H_C, T) points were extracted and are depicted in Fig. 6b. The H_c–T phase diagram reveals the presence of three distinct magnetic phases: a hidden spin-canted state, an antiferromagnetic (AFM) ordered state, and a paramagnetic state. The proposed magnetic structures corresponding to compounds **1** and **2** are illustrated in Fig. S6.†

Giant magnetocaloric effect

Specific heat measurements of compound **1** reveal a pronounced λ-shaped peak near 16 K under a zero magnetic field (Fig. 7a), indicative of a second-order magnetic phase transition. Upon the application of external magnetic fields, this peak gradually diminishes in intensity and shifts to lower temperatures, ultimately vanishing beyond 70 kOe (Fig. 7b),
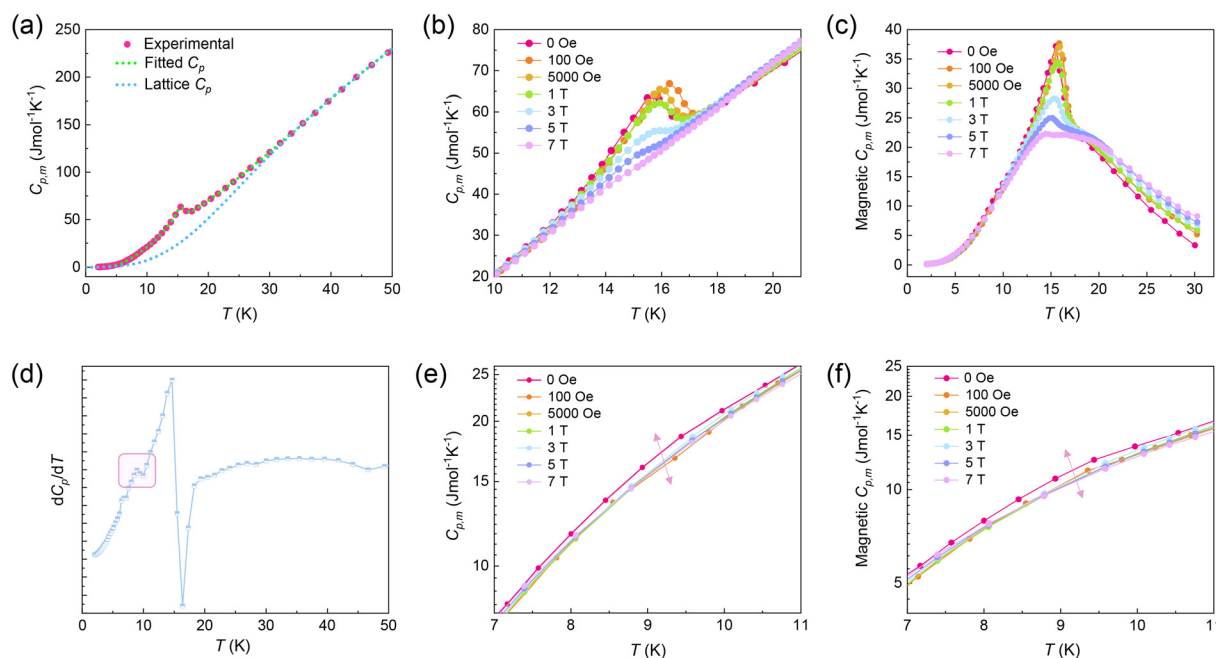
Fig. 7 (a) Variable temperature experimental (red line), fitted (green line), and lattice (blue line) heat-capacity plots of **1** under a 0 dc field. (b) Variable temperature heat-capacity plots of **1** under different dc fields. (c) Variable temperature magnetic heat-capacity plots of **1** under different dc fields. (d) The first derivative of variable temperature experimental heat-capacity plots of **1**. (e) The enlarged plots of (b) over the temperature range of 2–14 K. (f) The enlarged plots of (c) over the temperature range of 2–12 K.
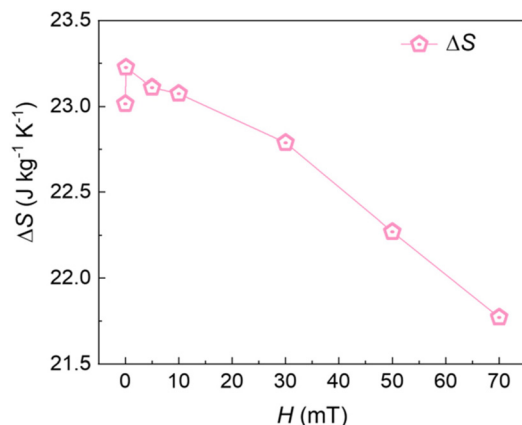
Fig. 8 The magnetic entropy changes ΔS of **1** under different magnetic fields.

thus confirming the presence of a long-range antiferromagnetic ordering and associated superparamagnetic behavior. Consistent trends are also observed in field-dependent magnetic specific heat data (Fig. 7c), further validating the magnetic phase transitions. Notably, the transition from a canted antiferromagnetic (AFM) phase to a more collinear AFM phase around 10 K is discernible in Fig. 7d (highlighted in pink) and is further supported by the magnified views in Fig. 7e and f. These specific heat observations are in excellent agreement with magnetic susceptibility data, corroborating a two-step magnetic phase transition.

The total entropy change in magnetic materials consists of lattice, magnetic, and electronic components, with only the magnetic entropy being field-dependent. Upon applying a magnetic field, spin alignment reduces magnetic entropy due to suppressed spin disorder. The magnetic contribution to entropy was determined by subtracting the lattice and electronic components using a composite Debye–Einstein model: $C_{p,m} = m \cdot D(\Theta_D/T) + n_1 \cdot E(\Theta_{E,1}/T) + n_1 \cdot E(\Theta_{E,2}/T)$, where $D(\Theta_D/T)$, $E(\Theta_{E,1}/T)$ and $E(\Theta_{E,2}/T)$ are the Debye and low and high temperature Einstein functions, respectively; m, n_1, n_2, Θ_D, $\Theta_{E,1}$, and $\Theta_{E,2}$ are adjustable parameters. The magnetic entropy change (ΔS) was calculated by integrating the magnetic specific heat curves under varying external fields (Fig. 8). At a zero field, ΔS reaches 23.16 J K^{-1} kg^{-1}, which increases sharply to a maximum of 23.22 J K^{-1} kg^{-1} under a low field of 100 Oe. With further increases in the magnetic field, ΔS gradually decreases. This field-dependent suppression of magnetic entropy suggests the presence of a magnetically frustrated ground state, which undergoes a field-induced transition from an antiferromagnetic to ferromagnetic alignment.

Conclusions

In summary, two cyano-bridged {Fe$_2$Co} molecular magnets featuring tunable topological architectures and interlayer interactions were successfully synthesized through the modulation of tricyanoferrate building blocks. In compound **1**, the Fe–Co units bridged by cyano ligands exhibit ferromagnetic coupling. The low-symmetry crystal structure permits the DM exchange interaction, leading to a noncollinear spin alignment between the Fe and Co centers and resulting in a canted antiferromagnetic ground state below 9 K. The weak interchain but relatively strong interlayer π⋯π stacking interactions suppress interchain magnetic communication while simultaneously contributing to a substantial magnetic phase transition field and a pronounced magnetocaloric entropy change. The field-induced magnetocaloric effect highlights the potential of compound **1** in magnetic refrigeration applications. In contrast, compound **2** exhibits antiferromagnetic coupling between Fe and Co centers, with its high-symmetry structure inhibiting spin canting. A magnetic phase transition is observed at a low magnetic field, corresponding to an interlayer antiferromagnetic-to-ferromagnetic transition, which is likely facilitated by weak interlayer interactions. These findings underscore the critical role of structural symmetry and intermolecular interactions in governing the magnetic exchange pathways and magnetic phase transitions.

Conflicts of interest

There are no conflicts to declare.

Data availability

The data supporting this article have been included as part of the ESI† and can be obtained freely upon request from the authors.

Acknowledgements

References

1 Y. Zhang, J. Zhu, S. Li, J. Wang and Z. Ren, *J. Mater. Sci. Technol.*, 2022, **102**, 66–71.

2 Y. Zhang, J. Zhu, S. Li, Z. Zhang, J. Wang and Z. Ren, *Sci. China Mater.*, 2022, **65**, 1345–1352.

3 X. Tang, H. Sepehri-Amin, N. Terada, A. Martin-Cid, I. Kurniawan, S. Kobayashi, Y. Kotani, H. Takeya, J. Lai, Y. Matsushita, T. Ohkubo, Y. Miura, T. Nakamura and K. Hono, *Nat. Commun.*, 2022, **13**, 1817.

4   L. I. Naumova, R. S. Zavornitsyn, M. A. Milyaev, M. V. Makarova, V. V. Proglyado and V. V. Ustinov, *IEEE Trans. Nanotechnol.*, 2021, **20**, 866–872.

5   M. Uehara, S. Mori, C. H. Chen and S.-W. Cheong, *Nature*, 1999, **399**, 560–563.

6   M. Sofronie, B. Popescu, M. Enculescu, M. Tolea and F. Tolea, *Nanomaterials*, 2022, **12**, 3667.

7   S. Jin, T. H. Tiefel, M. McCormack, R. A. Fastnacht, R. Ramesh and L. H. Chen, *Science*, 1994, **264**, 413–415.

8   S. Jiang, H. Xie, J. Shan and K. F. Mak, *Nat. Mater.*, 2020, **19**, 1295–1299.

9   D. Jiang, H. Zuo, Z. Zeng, H. Niu, Y. Liang, H. Huang, P. Yang, Z. Dong, Y. Sui, Y. Sun, Z. Ouyang and Z. Xia, *Phys. Rev. B*, 2024, **109**, 104418.

10 V. Khovaylo, I. Tereshina, G. Politova, A. Karpenkov, S. Taskaev and T. Palewski, *J. Alloys Compd.*, 2018, **741**, 689–692.

11 T. Sakon, K. Morikawa, Y. Narumi, M. Hagiwara, T. Kanomata, H. Nojiri and Y. Adachi, *Metals*, 2023, **13**, 1185.

12 Q. Meng, J. Dong, P. Nie, L. Xu, J. Wang, S. Jiang, H. Zuo, J. Zhang, X. Li, Z. Zhu, L. Balents and K. Behnia, *Nat. Commun.*, 2024, **15**, 6921.

13 J. K. Dey and S. Das, *Nat. Phys.*, 2024, **20**, 893–894.

14 L. Bai, W. Feng, S. Liu, L. Šmejkal, Y. Mokrousov and Y. Yao, *Adv. Funct. Mater.*, 2024, **34**, 2409327.

15 J. Y. Law, V. Franco, L. M. Moreno-Ramírez, A. Conde, D. Y. Karpenkov, I. Radulov, K. P. Skokov and O. Gutfleisch, *Nat. Commun.*, 2018, **9**, 2680.

16 M. Balli, S. Jandl, P. Fournier and A. Kedous-Lebouc, *Appl. Phys. Rev.*, 2017, **4**, 021305.

17 Y. Zhang, J. Zhu, S. Li, Z. Zhang, J. Wang and Z. Ren, *Sci. China Mater.*, 2022, **65**, 1345–1352.

18 V. Franco, J. S. Blázquez, J. J. Ipus, J. Y. Law, L. M. Moreno-Ramírez and A. Conde, *Prog. Mater. Sci.*, 2018, **93**, 112–232.

19 T. Gottschall, K. P. Skokov, M. Fries, A. Taubel, I. Radulov, F. Scheibel, D. Benke, S. Riegg and O. Gutfleisch, *Adv. Energy Mater.*, 2019, **9**, 1901322.

20 W. Deng, C.-Y. Yao, Y.-C. Chen, Y.-Q. Zhou, S.-N. Du, J.-L. Liu and M.-L. Tong, *Sci. China: Chem.*, 2024, **67**, 3291–3298.

21 H.-Y. Sun, P.-D. Mao, F.-F. Yan, X.-F. Li, R.-H. Zhou, Y.-S. Meng and T. Liu, *Cryst. Growth Des.*, 2023, **23**, 7939–7946.

22 E. Stryjewski and N. Giordano, *Adv. Phys.*, 1977, **26**, 487–650.

23 A. Ritchhart, A. S. Filatov, I.-R. Jeon and J. S. Anderson, *Inorg. Chem.*, 2023, **62**, 2817–2825.

24 Y.-Z. Zheng, W. Xue, M.-L. Tong, X.-M. Chen, F. Grandjean and G. J. Long, *Inorg. Chem.*, 2008, **47**, 4077–4087.

25 S. Wöhlert, J. Boeckmann, M. Wriedt and C. Näther, *Angew. Chem., Int. Ed.*, 2011, **50**, 6920–6923.

26 S. Wöhlert, Z. Tomkowicz, M. Rams, S. G. Ebbinghaus, L. Fink, M. U. Schmidt and C. Näther, *Inorg. Chem.*, 2014, **53**, 8298–8310.

27 S. W. Choi, H. Y. Kwak, J. H. Yoon, H. C. Kim, E. K. Koh and C. S. Hong, *Inorg. Chem.*, 2008, **47**, 10214–10216.

28 X.-B. Li, Y. Ma and E.-Q. Gao, *Inorg. Chem.*, 2018, **57**, 7446–7454.

29 J. Yang, X.-H. Zhao, Y.-F. Deng, X.-Y. Zhang, X.-Y. Chang, Z. Zheng and Y.-Z. Zhang, *Inorg. Chem.*, 2020, **59**, 16215–16224.

30 K. Nakabayashi, S. Chorazy, D. Takahashi, T. Kinoshita, B. Sieklucka and S. Ohkoshi, *Cryst. Growth Des.*, 2014, **14**, 6093–6100.

31 J. Yang, M.-L. You, S. Liu, Y.-F. Deng, X.-Y. Chang, S. M. Holmes and Y.-Z. Zhang, *Inorg. Chem.*, 2023, **62**, 17530–17536.

32 J. H. Yoon, J. H. Lim, S. W. Choi, H. C. Kim and C. S. Hong, *Inorg. Chem.*, 2007, **46**, 1529–1531.

33 S. W. Choi, H. Y. Kwak, J. H. Yoon, H. C. Kim, E. K. Koh and C. S. Hong, *Inorg. Chem.*, 2008, **47**, 10214–10216.

34 T. D. Harris, C. Coulon, R. Clérac and J. R. Long, *J. Am. Chem. Soc.*, 2011, **133**, 123–130.

35 L. V. Zorina, S. V. Simonov, V. D. Sasnovskaya, A. D. Talantsev, R. B. Morgunov, V. S. Mironov and E. B. Yagubskii, *Chem. – Eur. J.*, 2019, **25**, 14583–14597.

36 D. Shao, S.-L. Zhang, X.-H. Zhao and X.-Y. Wang, *Chem. Commun.*, 2015, **51**, 4360–4363.

37 H.-R. Wen, C.-F. Wang, Y. Song, S. Gao, J.-L. Zuo and X.-Z. You, *Inorg. Chem.*, 2006, **45**, 8942–8949.

38 H. Zheng, *Nat. Commun.*, 2013, 1–7.

39 T. Liu, Y.-J. Zhang, S. Kanegawa and O. Sato, *J. Am. Chem. Soc.*, 2010, **132**, 8250–8251.

40 H.-R. Wen, C.-F. Wang, Y. Song, S. Gao, J.-L. Zuo and X.-Z. You, *Inorg. Chem.*, 2006, **45**, 8942–8949.

41 A. J. Howarth, T. C. Wang, S. S. Al-Juaid, S. G. Aziz, J. T. Hupp and O. K. Farha, *Dalton Trans.*, 2016, **45**, 93–97.

42 J. H. Yoon, J. H. Lim, S. W. Choi, H. C. Kim and C. S. Hong, *Inorg. Chem.*, 2007, **46**, 1529–1531.

43 T. D. Harris, C. Coulon, R. Clérac and J. R. Long, *J. Am. Chem. Soc.*, 2011, **133**, 123–130.